nature electronics

SUPPLEMENTARY INFORMATION
https://doi.org/10.1038/s41928-019-0247-9

In the format provided by the authors and unedited.

A flexible phased array system with low areal mass density

Mohammed Reza M. Hashemi[1*], Austin C. Fikes[1], Matan Gal-Katziri[1], Behrooz Abiri[1,2], Florian Bohn[1,2], Amirreza Safaripour[1,2], Michael D. Kelzenberg[3], Emily L. Warmann[3], Pilar Espinet[3], Nina Vaidya[3], Eleftherios E. Gdoutos[4], Christophe Leclerc[4], Fabien Royer[4], Sergio Pellegrino[4], Harry A. Atwater[3] and Ali Hajimiri[1]

[1]Department of Electrical Engineering, California Institute of Technology, Pasadena, CA, USA. [2]Auspion Inc., Pasadena, California, USA. [3]Department of Applied Physics and Materials Science, California Institute of Technology, Pasadena, CA, USA. [4]Graduate Aerospace Laboratories, California Institute of Technology, Pasadena, CA, USA. *e-mail: mreza@caltech.edu

a

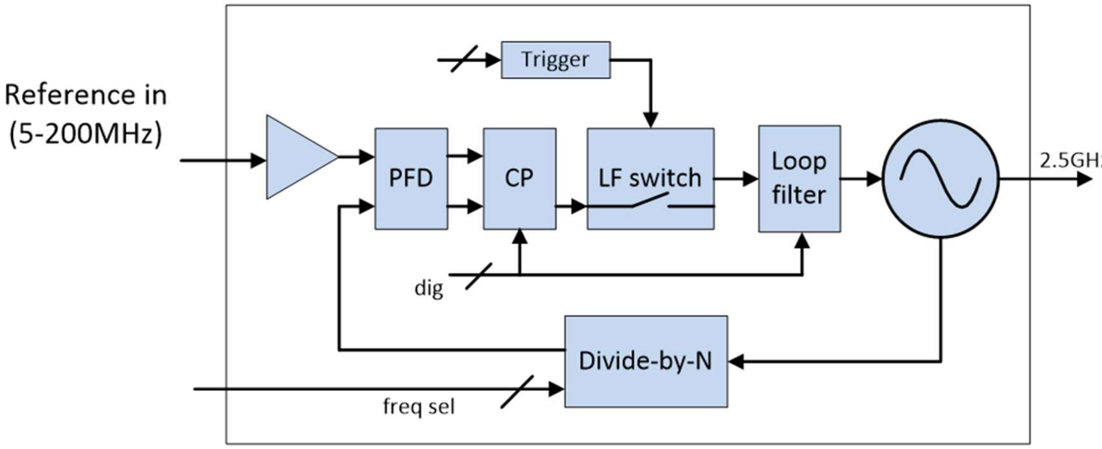

b

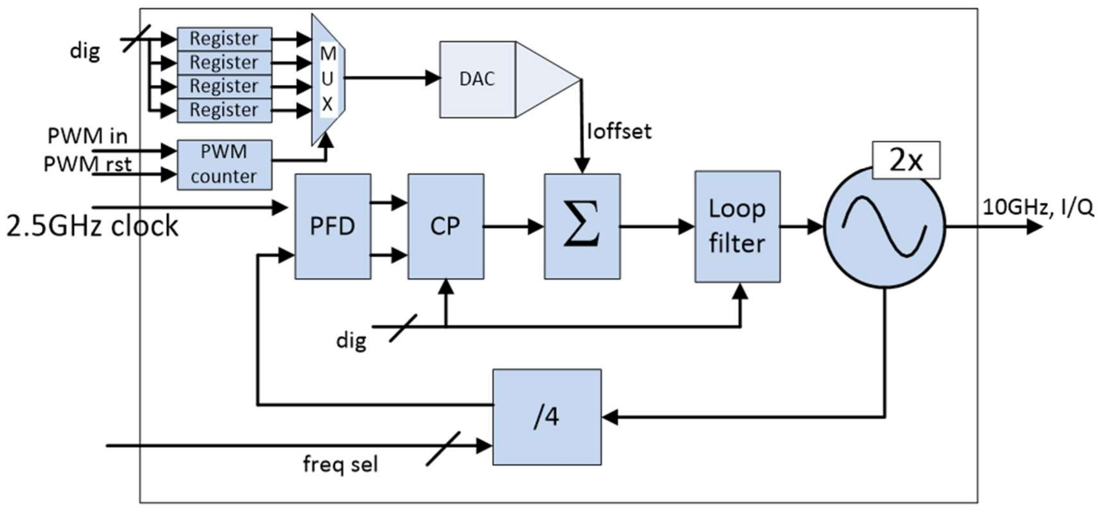

Supplementary Fig. 1 | Top level PSCU block diagram. a, The 2.5 GHz PLL. The output is distributed across the IC to its 16 output PAs. **b,** The clock multiplier unit (CMU) which synthesizes a phase-shifted 10 GHz signal for the output PAs.

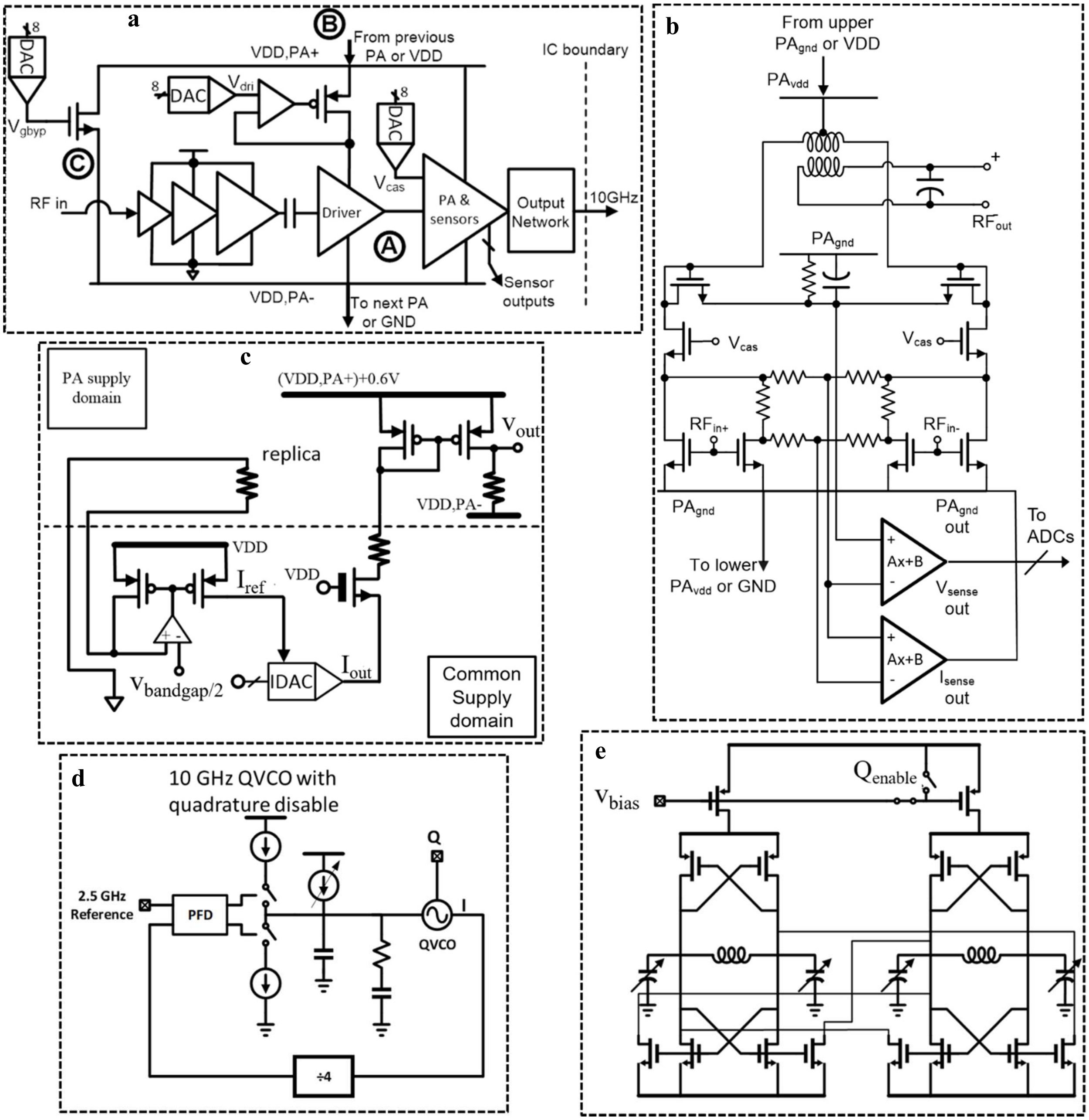

Supplementary Fig. 2 | Circuit model blocks of the X-band power amplifier quad RFIC. **a**, Power core implementation. **b,** PA core sensors. **c,** Process, voltage and temperature (PVT) independent bias generator. **d,** The 10 GHz phase locked loop (PLL). **e,** The PLL's quadrature voltage controlled oscillator (QVCO).

a

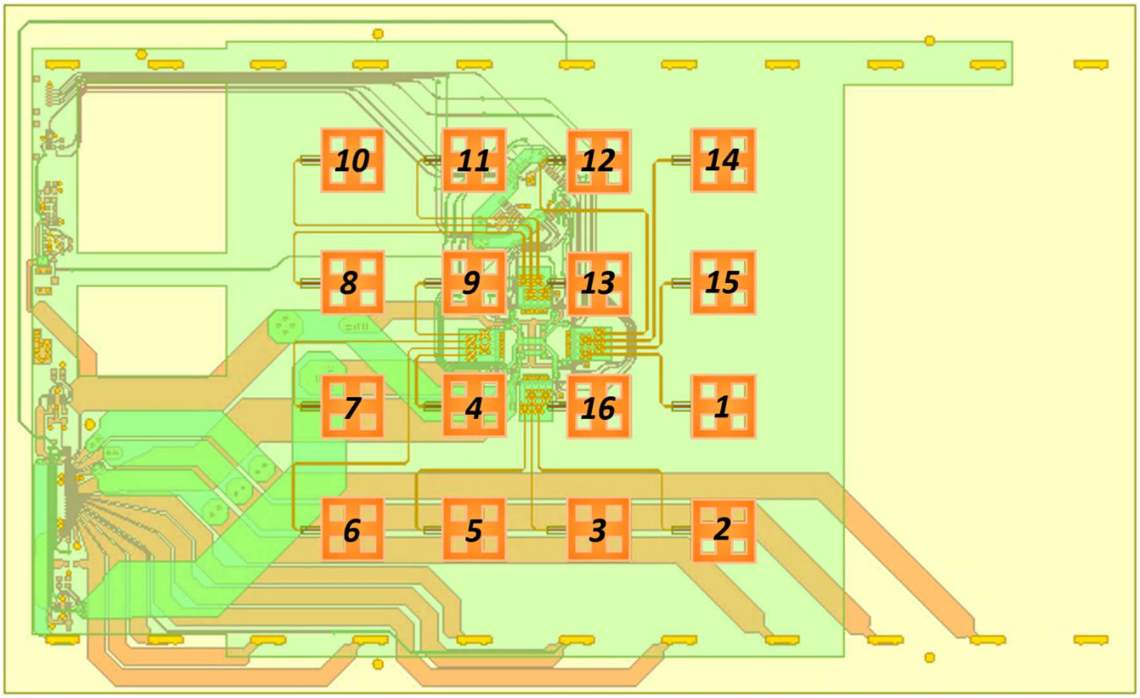

b

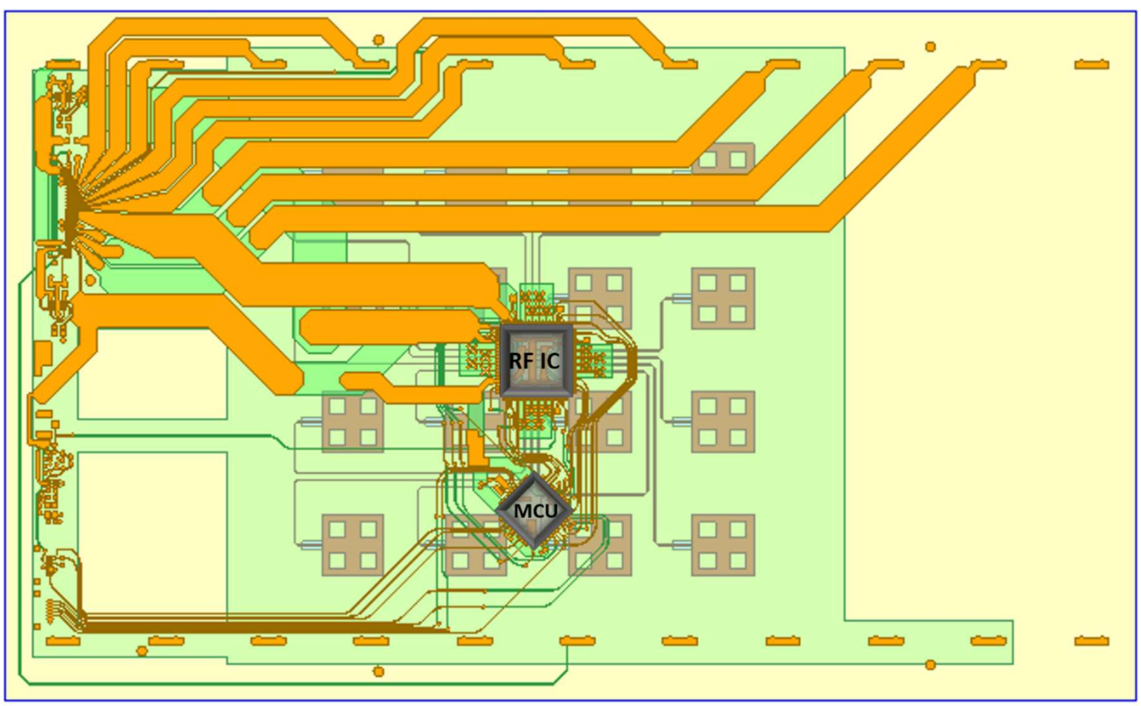

Supplementary Fig. 3 | Detail layout of a 4x4 ultra-lightweight collapsible and deployable phased array system that is integrated with photovoltaics solar cells and concentrators. a, The radiator side. **b**, The RF IC side.

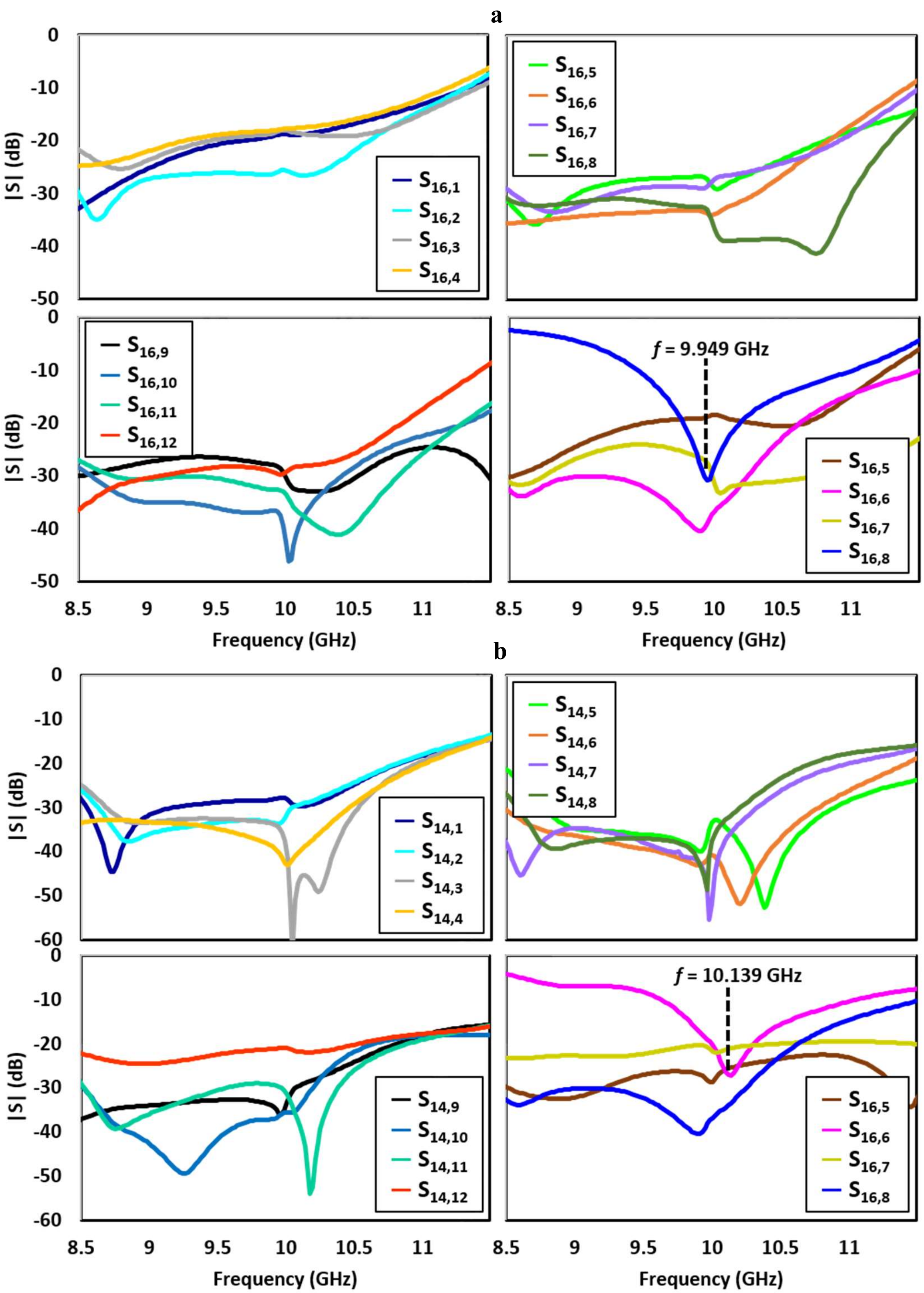

Supplementary Fig. 4 | The 4x4 flexible phased array system prototype simulated scattering parameters. a, Frequency responses due to element 16 being excited (member of the outer 12 radiating elements). **b,** Frequency responses due to element 14 being excited (member of the inner 4 radiating elements). For the ease of visualization every four S-parameter curves are shown in a separate plot. Element numbering is referenced to supplementary Fig. 3.

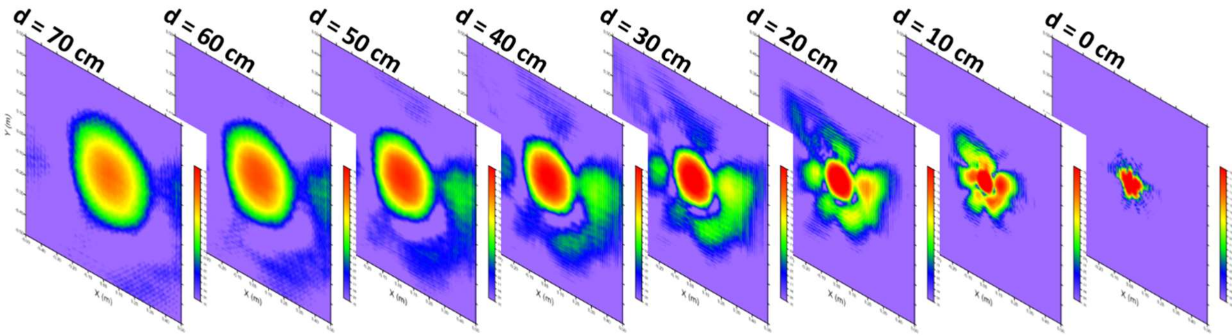

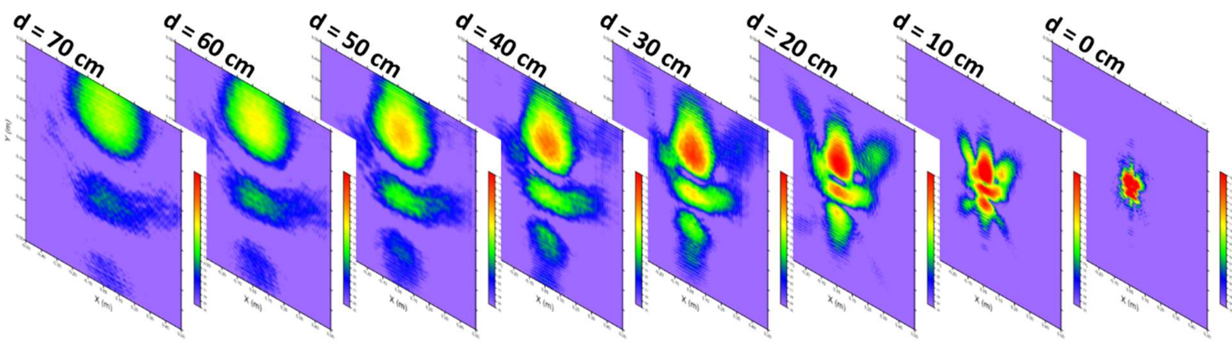

Supplementary Fig. 5 | Measured hologram plots for the 4x4 flexible phased array tile prototype at *f* = 9.8 GHz over different *xy*-plane cross-sections along the *z*-direction (propagation direction) for every 10 cm of propagation when all 16-elements turned ON and their phases are optimized for. a, Scan angle (φ = 0°, θ = 0°). **b,** Scan angle (φ = 90°, θ = 30°).

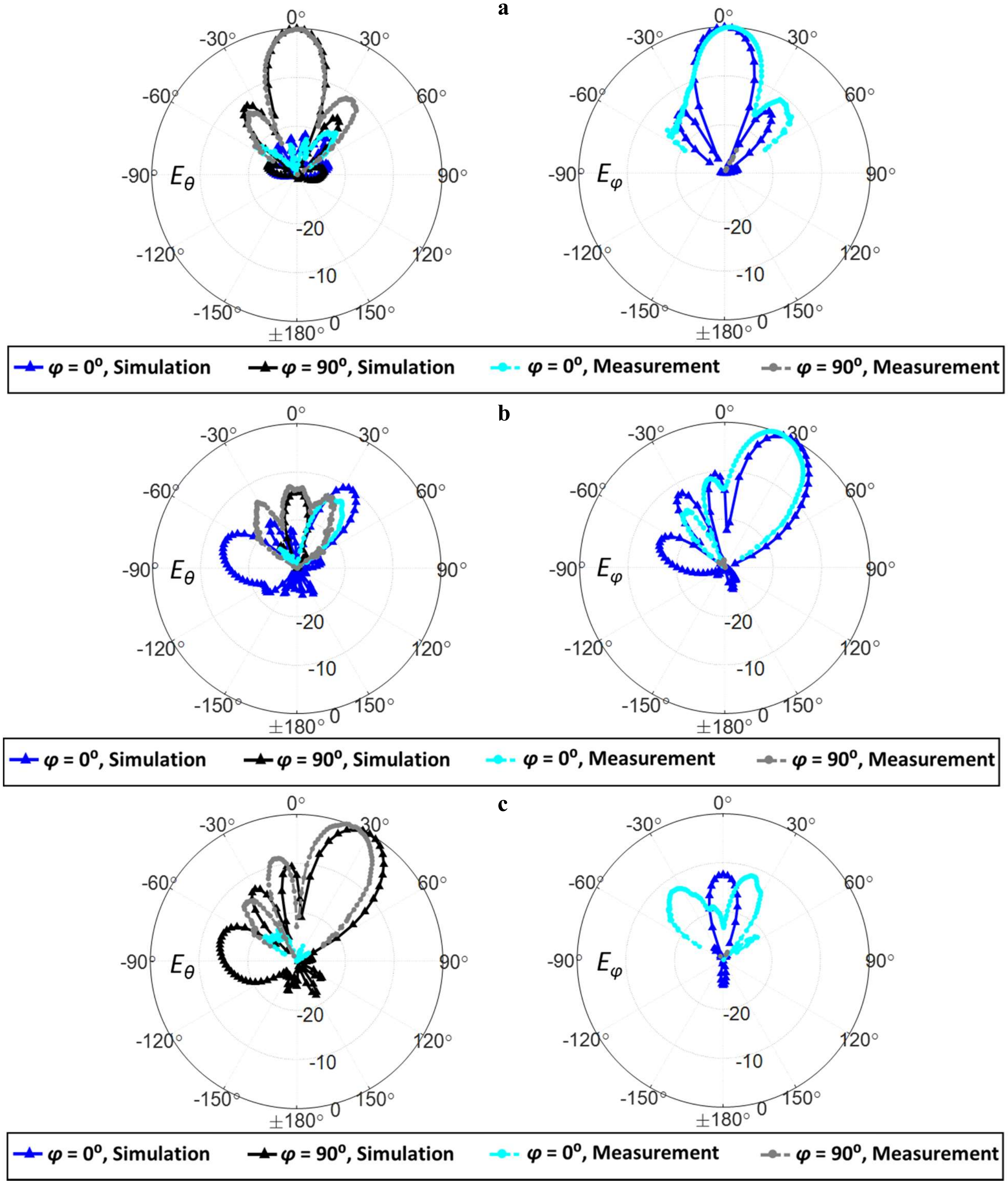

Supplementary Fig. 6 | Simulated and measured far-field radiation patterns of the E_θ (left column plots) and E_φ (right column plots) components of the radiated *E*-fields of the 4x4 flexible phased array tile prototype at *f* = 9.8GHz along the *E*-plane (φ = 90°) and the *H*-plane (φ = 0°) for three scan angels. a, (φ = 0°, θ = 0°). **b,** (φ = 0°, θ = 30°). **c,** (φ = 90°, θ = 30°).

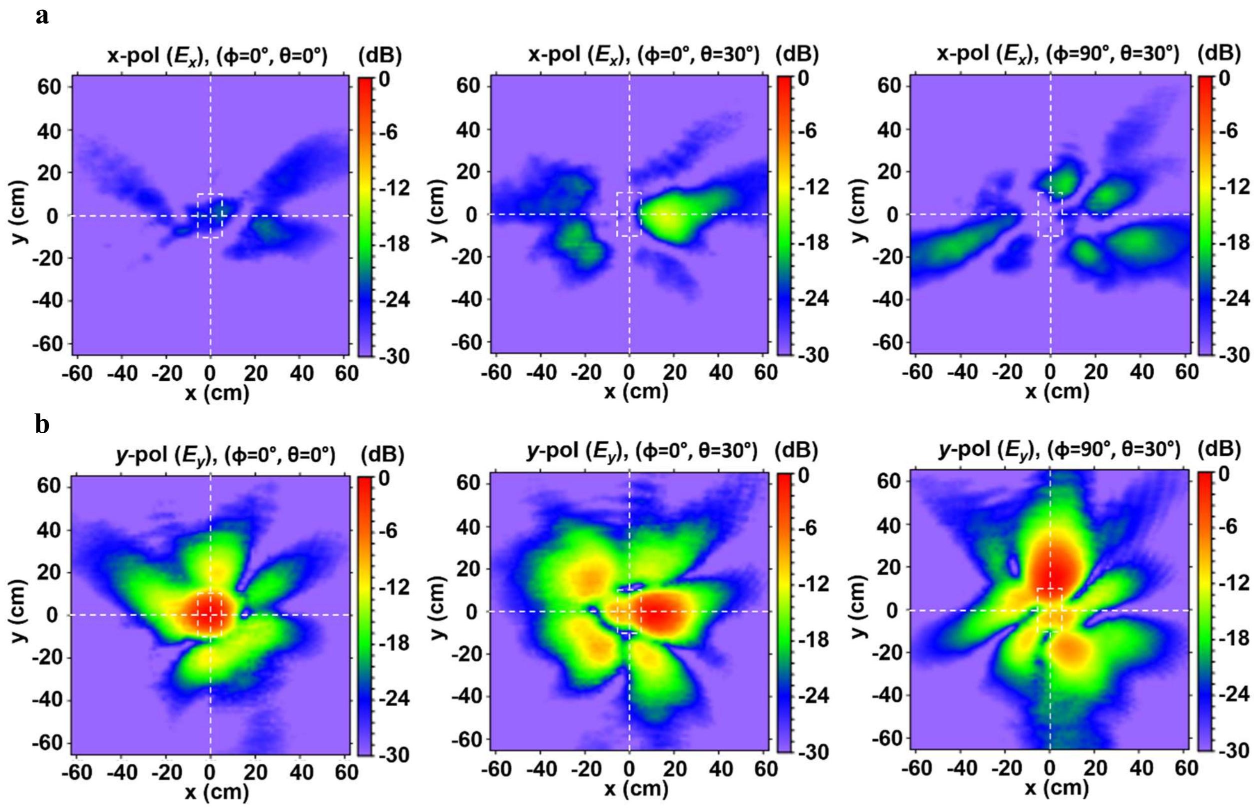

Supplementary Fig. 7 | Near-filed measurement of the 4x4 flexible phased array tile prototype when 12 elements are active and 4 corner elements are turned OFF at *f* = 9.8 GHz. **a,** Cross-polarization near-field component of *E*-field (E_x). **b,** Co-polarization near-field component of *E*-field (E_y), for three scan angels (φ = 0°, θ = 0°), (φ = 0°, θ = 30°), and (φ = 90°, θ = 30°) shown from left to right.

a

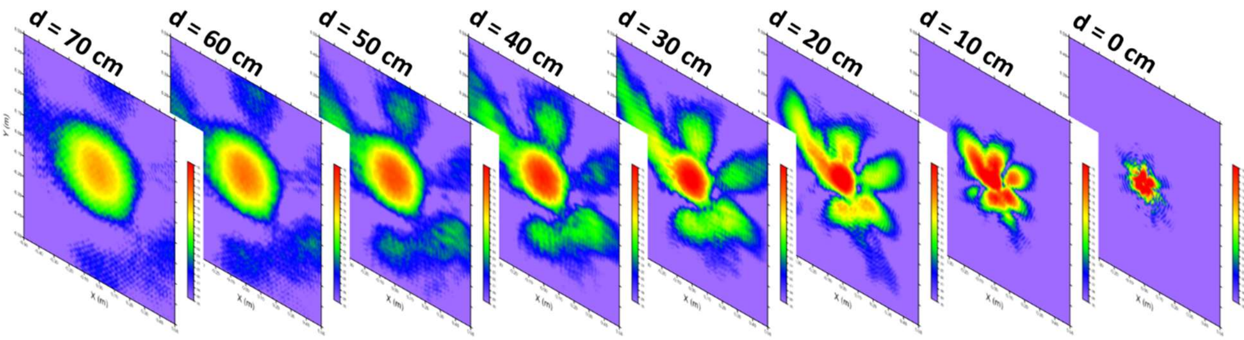

b

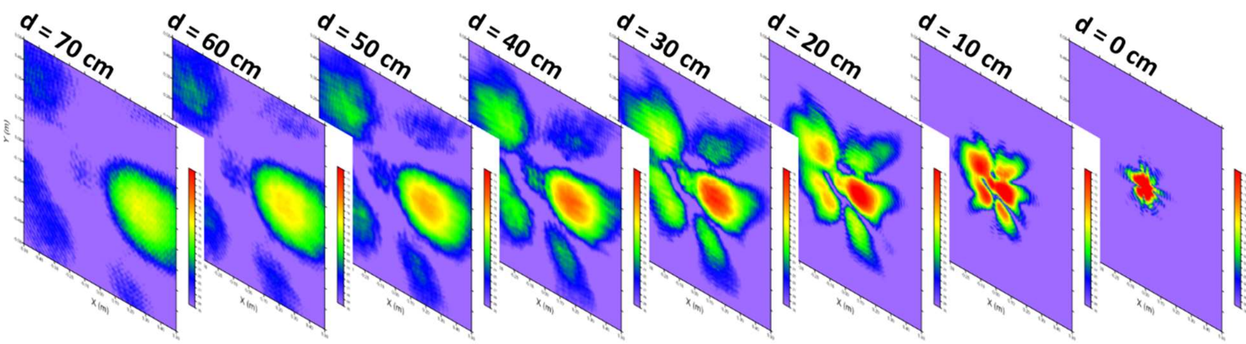

c

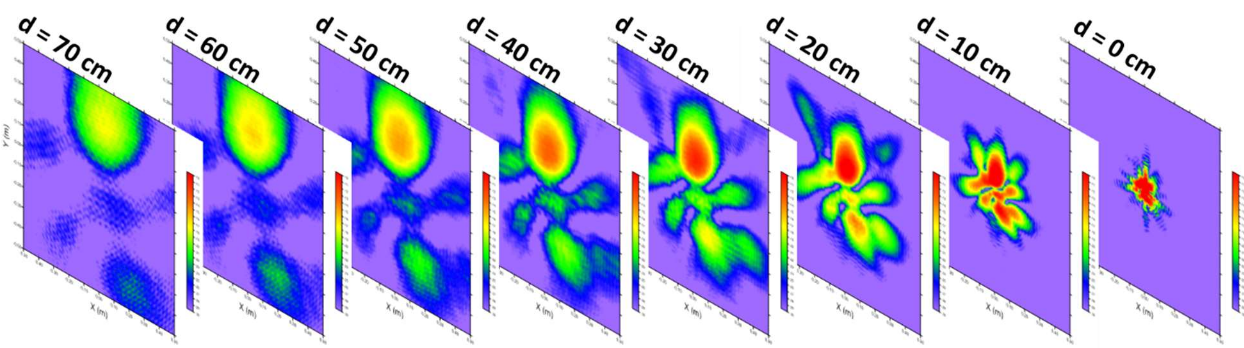

Supplementary Fig. 8 | Measured hologram plots for the 4x4 flexible phased array tile prototype at f = 9.8 GHz over different *xy*-plane cross-sections along the z-direction (propagation direction) for every 10 cm of propagation when 12 elements are active and 4 corner elements are turned OFF. a, Phases are optimized for scan angle ($\varphi = 0°$, $\theta = 0°$). **b,** Phases are optimized for scan angle ($\varphi = 0°$, $\theta = 30°$). **c,** Phases are optimized for scan angle ($\varphi = 90°$, $\theta = 30°$).

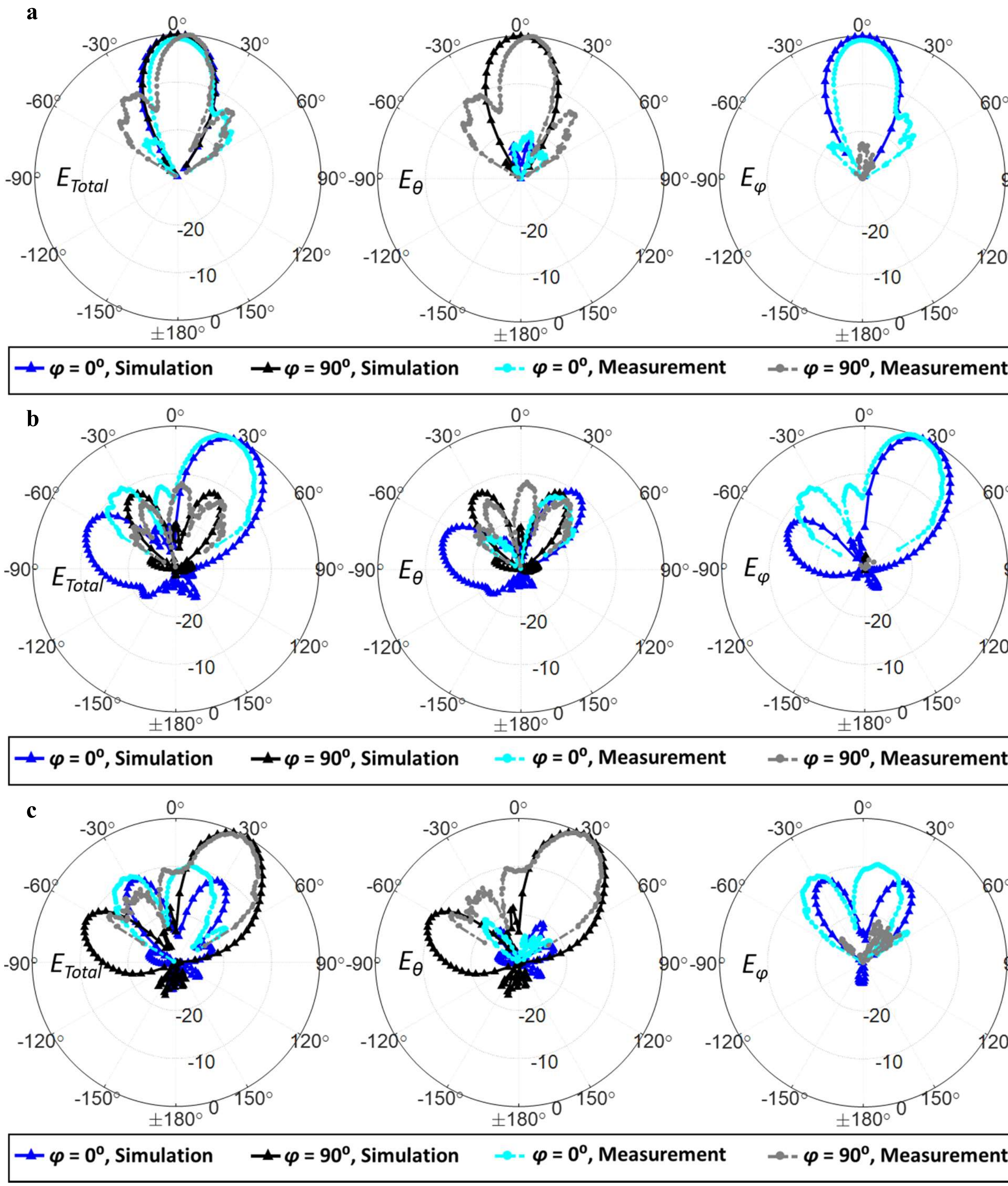

Supplementary Fig. 9 | Simulated and measured far-field radiation patterns of the total radiated *E*-field (left column plots), E_θ component (middle column plots) and E_φ component (right column plots) of the 4x4 flexible phased array tile prototype at f = 9.8 GHz along the *E*-plane (φ = 90°) and the *H*-plane (φ = 0°) for three scan angels when 12 elements are active and 4 corner elements are turned OFF. a, Scan angle (φ = 0°, θ = 0°). **b,** Scan angle (φ = 0°, θ = 30°). **c.** Scan angle (φ = 90°, θ = 30°).

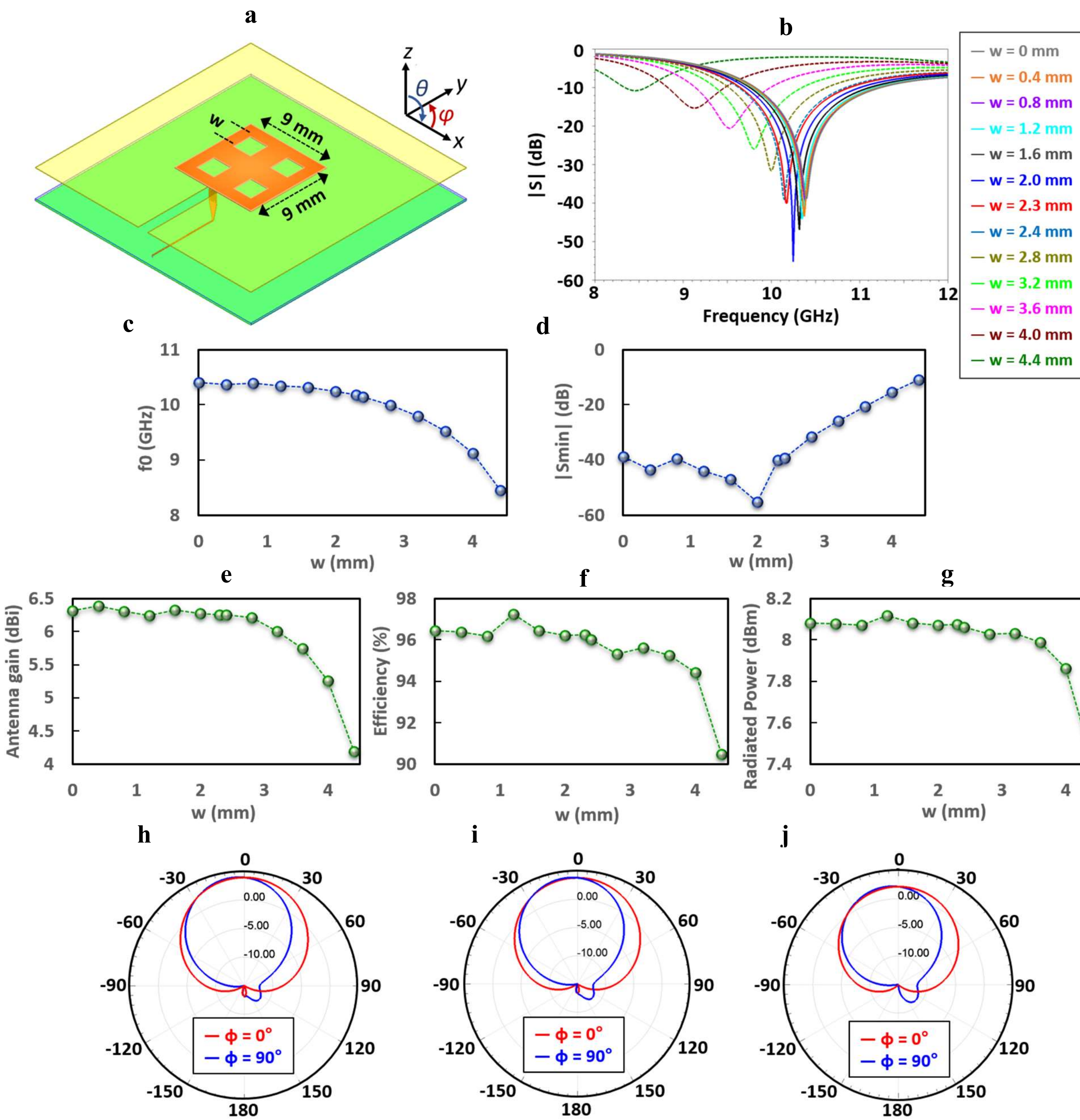

Supplementary Fig. 10 | Investigation of square cutout effect on the performance of the flexible fractal inspired modified patch radiator. ,. Schematic of the antenna. **b,** Reflection coefficient of the antenna for different square cutout widths. **c,** Antenna resonance frequency as a function of square cutout widths. **d,** Minimum return loss value (impedance matching condition) at the antenna resonance frequency as a function of square cutout widths. **e,** Antenna gain at the antenna resonance frequency as a function of square cutout widths. **f,** Antenna radiation efficiency at the antenna resonance frequency as a function of square cutout widths. **g,** Antenna radiated power at the antenna resonance frequency as a function of square cutout widths. **h,** Far-field radiation pattern of the total radiated *E*-field along $\varphi = 0°$ cut (red curve) and $\varphi = 90°$ cut (blue curve) for $w = 0$ mm at $f = 10.4$ GHz (antenna resonance frequency). **i,** Total radiated *E*-field radiation pattern along $\varphi = 0°$ cut (red curve) and $\varphi = 90°$ cut (blue curve) for $w = 2.3$ mm at $f = 10.14$ GHz (antenna resonance frequency). **j,** Total radiated *E*-field radiation pattern along $\varphi = 0°$ cut (red curve) and $\varphi = 90°$ cut (blue curve) for $w = 4$ mm at $f = 9.13$ GHz (antenna resonance frequency).

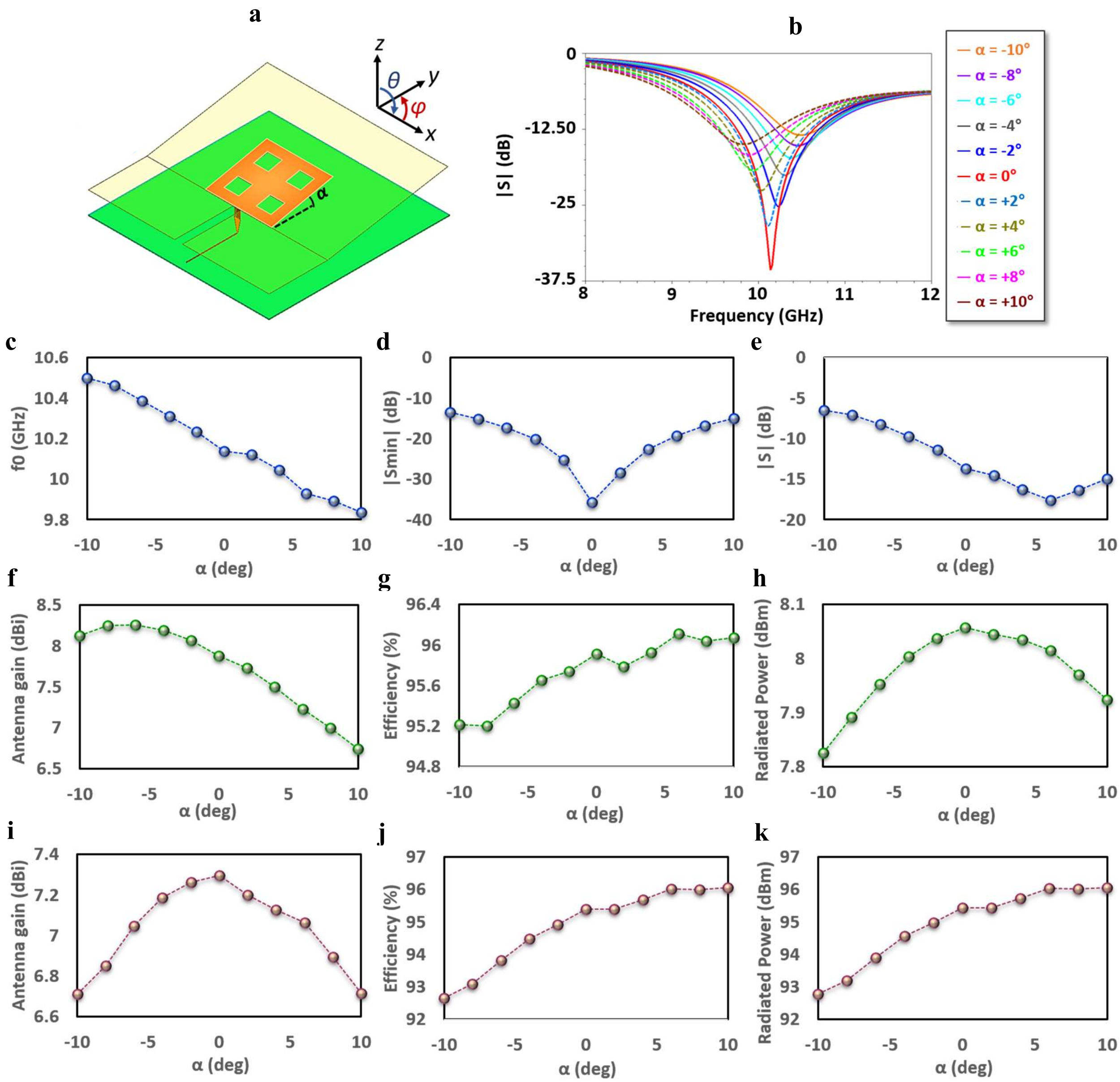

Supplementary Fig. 11 | Radiator layer pitch sensitivity analysis on the performance of the fractal inspired modified patch radiation for various pitch angle α measured from the *y*-axis. **a,** Schematic of the antenna. **b,** Return loss frequency response for different pitch angles. **c,** Antenna resonance frequency as a function of pitch angle at the corresponding resonance frequency. **d,** Minimum return loss value (impedance matching condition) as a function of pitch angle at the corresponding resonance frequency. **e,** Return loss value as a function of pitch angle at $f = 9.8$ GHz. **f,** Antenna gain as a function of pitch angle at the corresponding resonance frequency. **g,** Antenna radiation efficiency as a function of pitch angle at the corresponding resonance frequency. **h,** Radiated power as a function of pitch angle at the corresponding resonance frequency. **i,** Antenna gain as a function of pitch angle at $f = 9.8$ GHz. **j,** Antenna radiation efficiency as a function of pitch angle at $f = 9.8$ GHz. **k,** Radiated power as a function of pitch angle at $f = 9.8$ GHz.

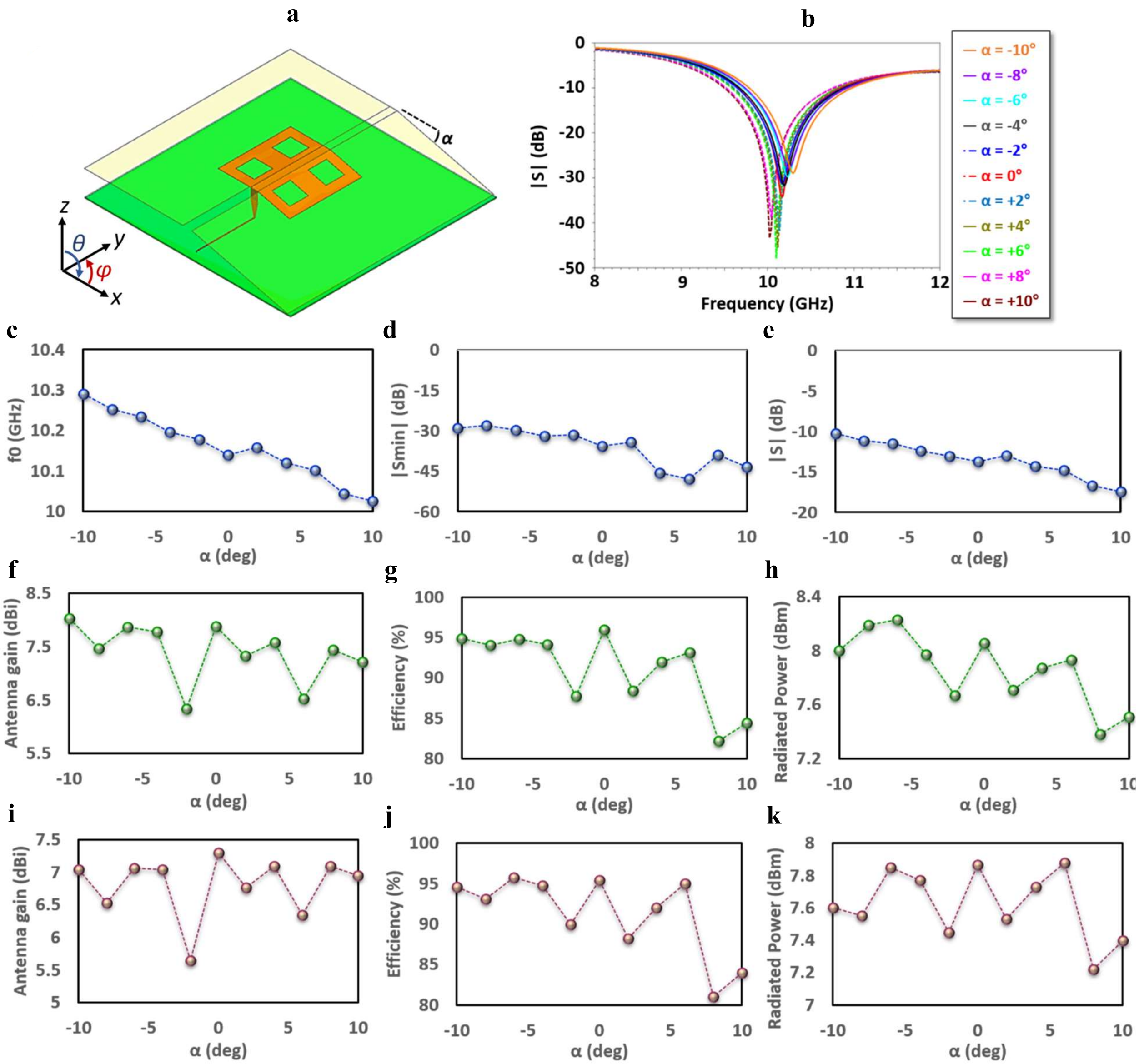

Supplementary Fig. 12 | Radiator layer single-side bend sensitivity analysis on the performance of the fractal inspired modified patch radiation for various single-side bend angle α measured from the *x*-axis. **a,** Schematic of the antenna. **b,** Return loss frequency response for different single-side bend angles. **c,** Antenna resonance frequency as a function of single-side bend angle at the corresponding resonance frequency. **d,** Minimum return loss value (impedance matching condition) as a function of single-side bend angle at the corresponding resonance frequency. **e,** Return loss value as a function of single-side bend angle at f = 9.8 GHz. **f,** Antenna gain as a function of single-side bend angle at the corresponding resonance frequency. **g,** Antenna radiation efficiency as a function of single-side bend angle at the corresponding resonance frequency. **h,** Radiated power as a function of single-side bend angle at the corresponding resonance frequency. **i,** Antenna gain as a function of single-side bend angle at f = 9.8 GHz. **j,** Antenna radiation efficiency as a function of single-side bend angle at f = 9.8 GHz. **k,** Radiated power as a function of single-side bend angle at f = 9.8 GHz.

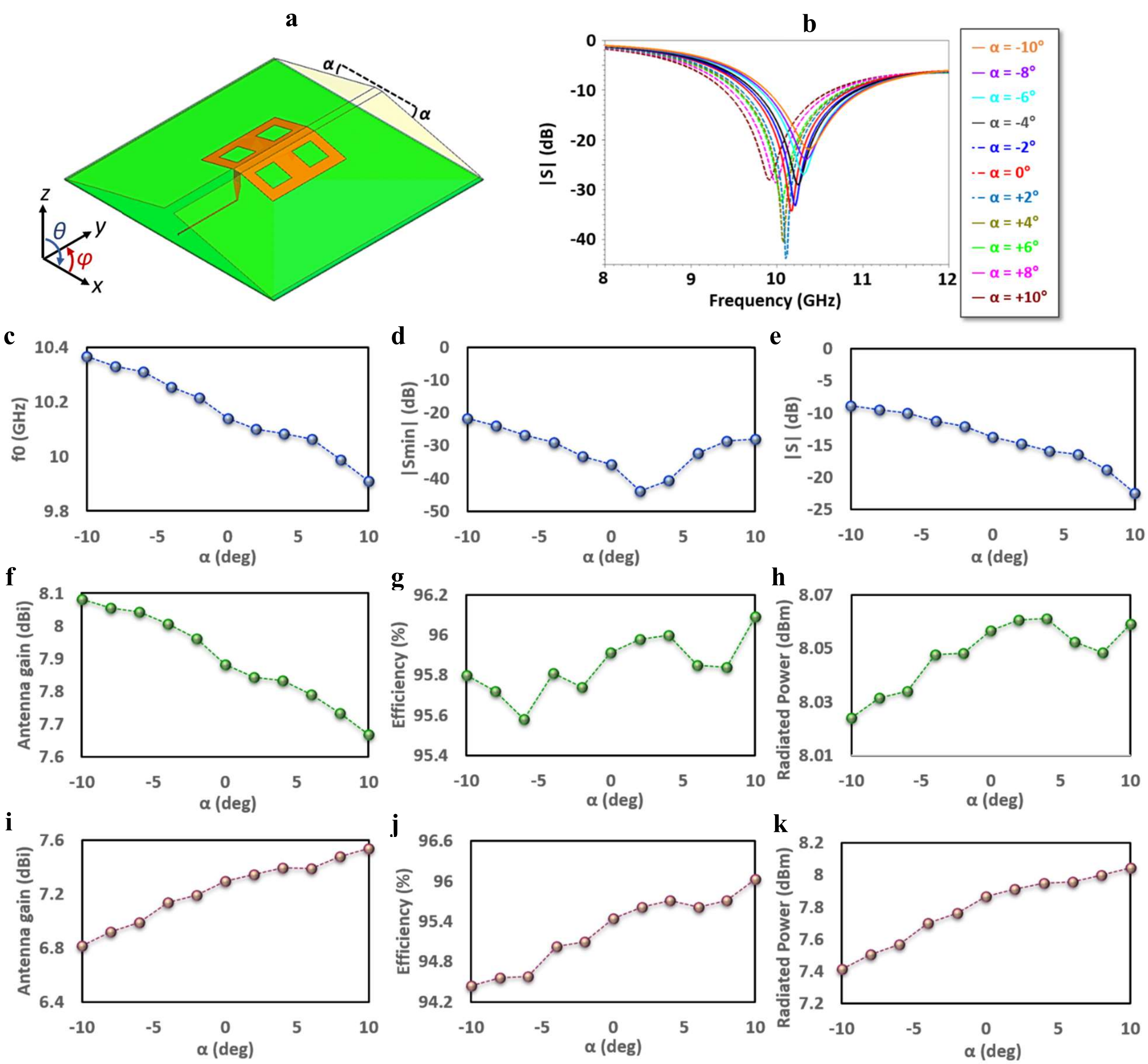

Supplementary Fig. 13 | Radiator layer double-side bend sensitivity analysis on the performance of the fractal inspired modified patch radiation for various double-side bend angle α measured from the *x*-axis. **a,** Schematic of the antenna. **b,** Return loss frequency response for different double-side bend angles. **c,** Antenna resonance frequency as a function of double-side bend angle at the corresponding resonance frequency. **d,** Minimum return loss value (impedance matching condition) as a function of double-side bend angle at the corresponding resonance frequency. **e,** Return loss value as a function of double-side bend angle at $f = 9.8$ GHz, **f.** antenna gain as a function of double-side bend angle at the corresponding resonance frequency. **g,** Antenna radiation efficiency as a function of double-side bend angle at the corresponding resonance frequency. **h,** Radiated power as a function of double-side bend angle at the corresponding resonance frequency. **i,** Antenna gain as a function of double-side bend angle at $f = 9.8$ GHz. **j,** Antenna radiation efficiency as a function of double-side bend angle at $f = 9.8$ GHz. **k,** Radiated power as a function of double-side bend angle at $f = 9.8$ GHz.

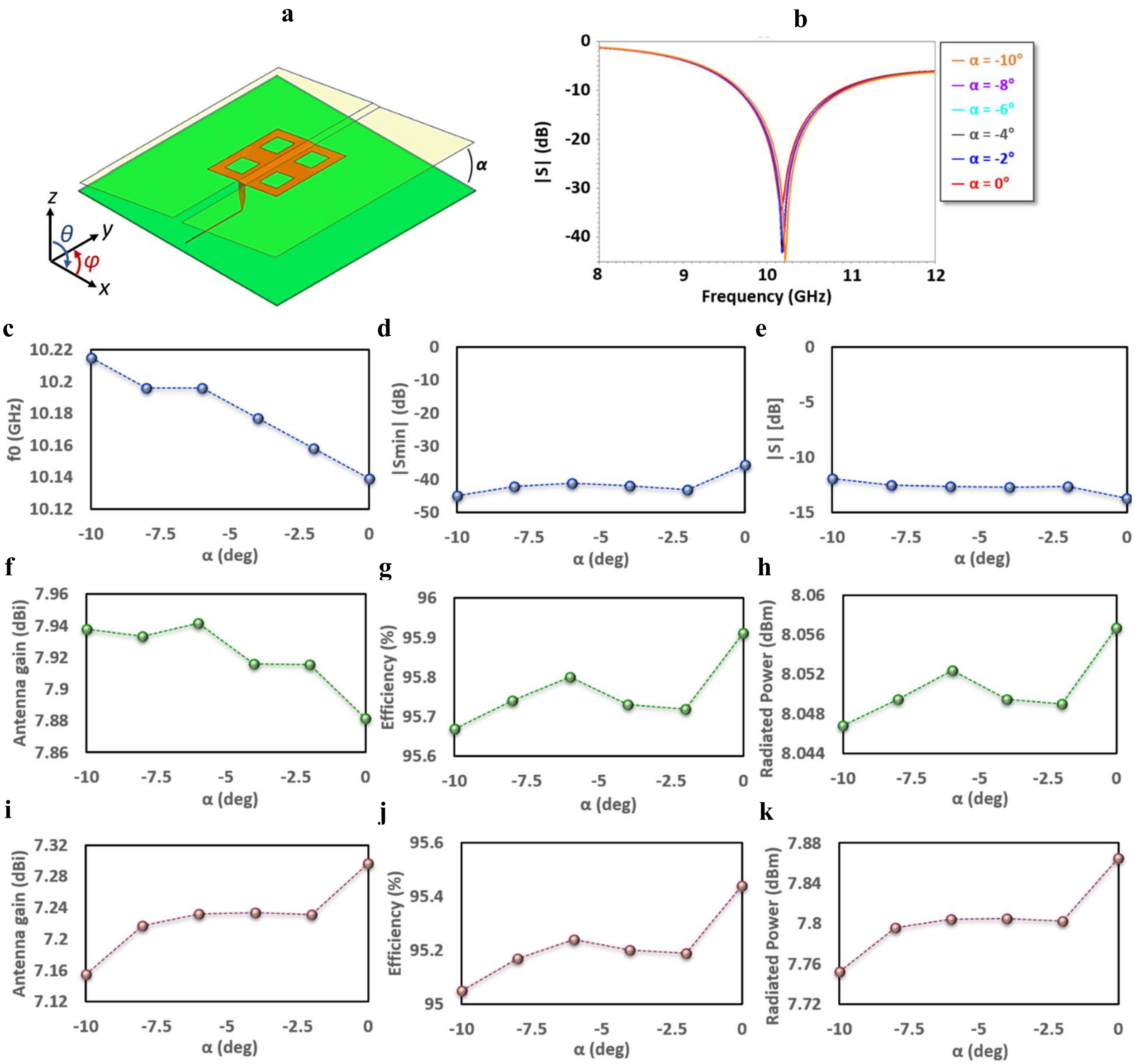

Supplementary Fig. 14 | Radiator layer tilt sensitivity analysis on the performance of the fractal inspired modified patch radiation for various tilt angle α measured from the *x*-axis. **a,** Schematic of the antenna. **b,** Return loss frequency response for different tilt angles. **c,** Antenna resonance frequency as a function of tilt angle at the corresponding resonance frequency. **d,** Minimum return loss value (impedance matching condition) as a function of tilt angle at the corresponding resonance frequency. **e,** Return loss value as a function of tilt angle at $f = 9.8$ GHz. **f,** Antenna gain as a function of tilt angle at the corresponding resonance frequency. **g,** Antenna radiation efficiency as a function of tilt angle at the corresponding resonance frequency. **h,** Radiated power as a function of tilt angle at the corresponding resonance frequency. **i,** Antenna gain as a function of tilt angle at $f = 9.8$ GHz. **j,** Antenna radiation efficiency as a function of tilt angle at $f = 9.8$ GHz. **k,** Radiated power as a function of tilt angle at $f = 9.8$ GHz.

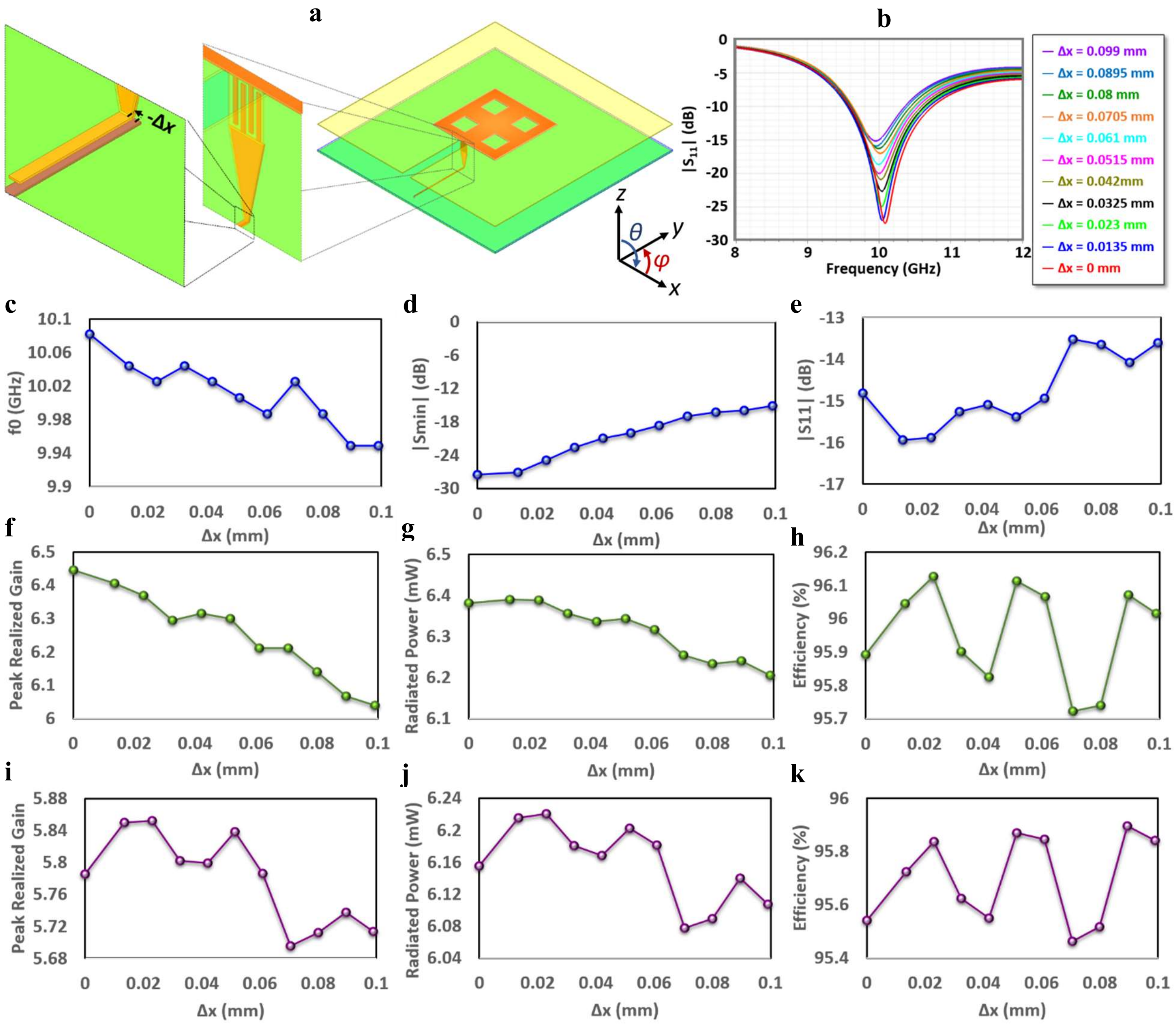

Supplementary Fig. 15 | Misalignment sensitivity analysis on the performance of the fractal inspired modified patch radiation for when the radiator layer and the 4-layer RF flexible board are misaligned in the *x*-direction. **a,** Schematic of the antenna. **b,** Return loss frequency response as a function of Δ*x*. **c,** Antenna resonance frequency as a function of Δ*x* at the corresponding resonance frequency. **d,** Minimum return loss value (impedance matching condition) as a function of Δ*x* at the corresponding resonance frequency. **e,** Return loss value as a function of Δ*x* at *f* = 9.8 GHz. **f,** Antenna gain as a function of Δ*x* at the corresponding resonance frequency. **g,** Radiated power as a function of Δ*x* at the corresponding resonance frequency. **h,** Antenna radiation efficiency as a function of Δ*x* at the corresponding resonance frequency. **i,** Antenna gain as a function of Δ*x* at *f* = 9.8 GHz. **j,** Radiated power as a function of Δ*x* at *f* = 9.8 GHz, **k,** Antenna radiation efficiency as a function of Δ*x* at *f* = 9.8 GHz.

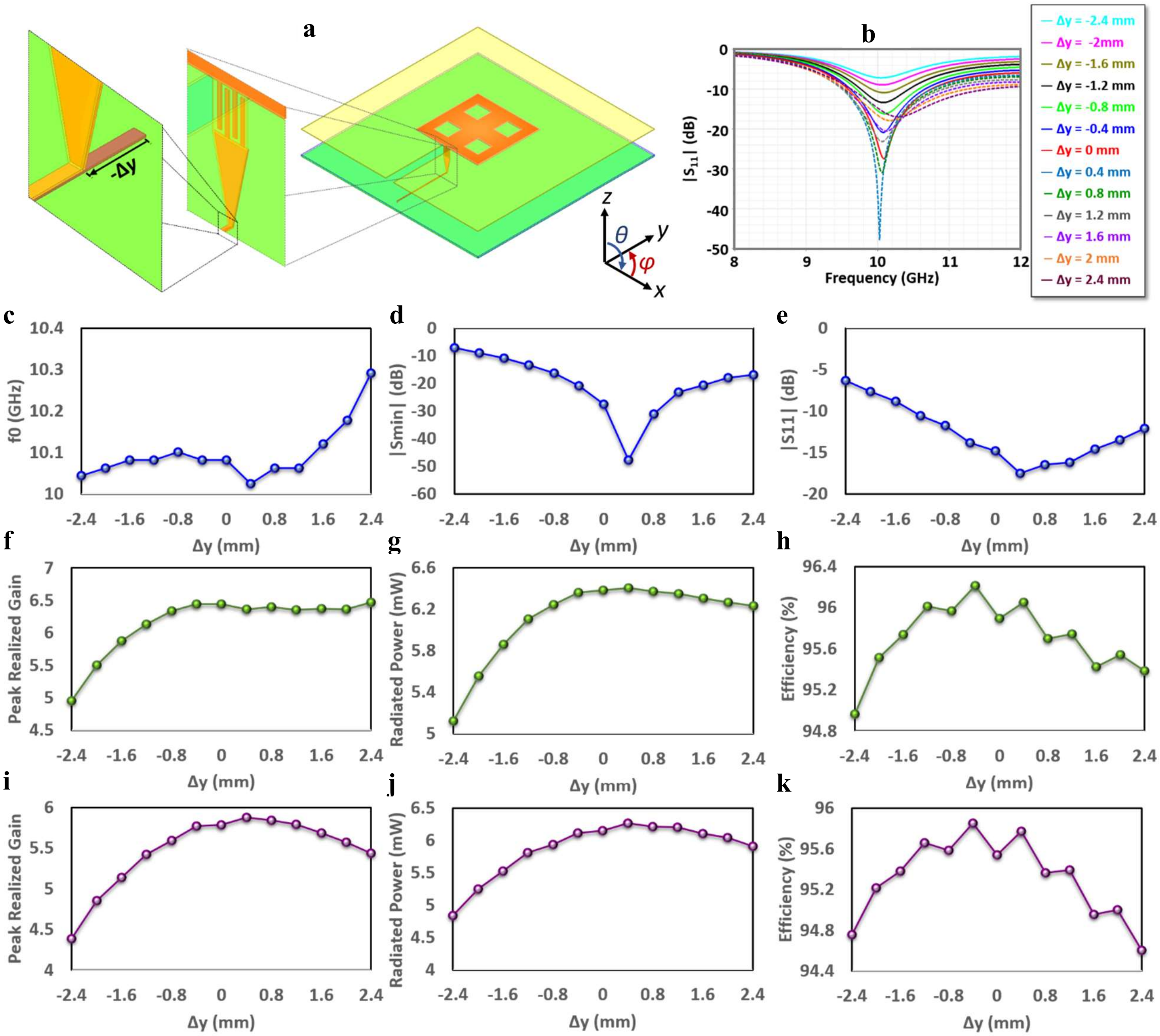

Supplementary Fig. 16 | Misalignment sensitivity analysis on the performance of the fractal inspired modified patch radiation for when the radiator layer and the 4-layer RF flexible board are misaligned in the *y*-direction. **a,** Schematic of the antenna. **b,** Return loss frequency response as a function of Δ*y*. **c,** Antenna resonance frequency as a function of Δ*y* at the corresponding resonance frequency. **d,** Minimum return loss value (impedance matching condition) as a function of Δ*y* at the corresponding resonance frequency. **e,** Return loss value as a function of Δ*y* at *f* = 9.8 GHz. **f,** Antenna gain as a function of Δ*y* at the corresponding resonance frequency. **g,** Radiated power as a function of Δ*y* at the corresponding resonance frequency. **h,** Antenna radiation efficiency as a function of Δ*y* at the corresponding resonance frequency. **i,** Antenna gain as a function of Δ*y* at *f* = 9.8 GHz. **j,** Radiated power as a function of Δ*x* at *f* = 9.8 GHz. **k,** Antenna radiation efficiency as a function of Δ*y* at *f* = 9.8 GHz.

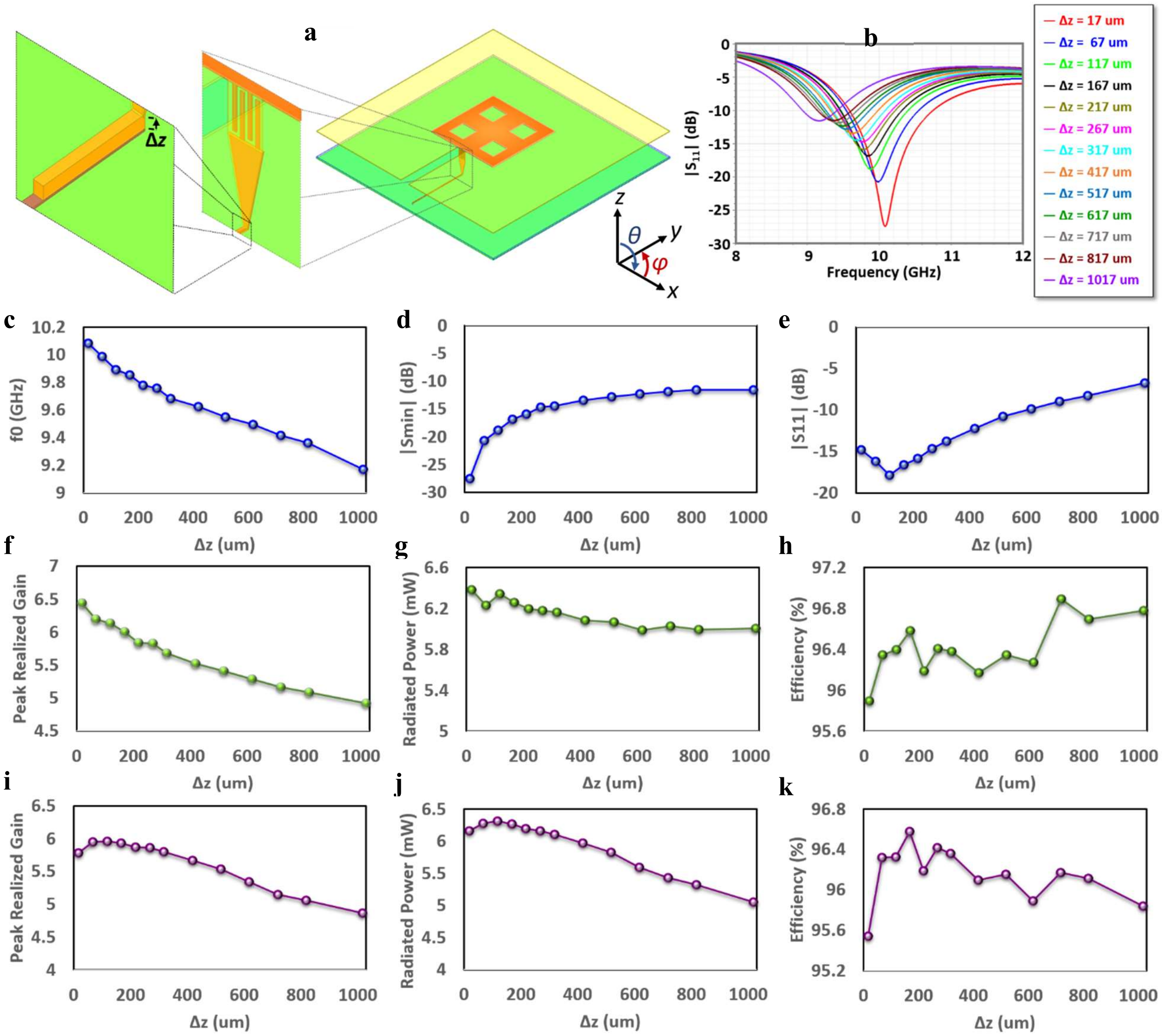

Supplementary Fig. 17 | Misalignment sensitivity analysis on the performance of the fractal inspired modified patch radiation for when the radiator layer and the 4-layer RF flexible board are misaligned in the *z*-direction (e.g. solder thickness). **a,** Schematic of the antenna. **b,** Return loss frequency response as a function of Δz. **c,** Antenna resonance frequency as a function of Δz at the corresponding resonance frequency. **d,** Minimum return loss value (impedance matching condition) as a function of Δz at the corresponding resonance frequency. **e,** Return loss value as a function of Δz at f = 9.8 GHz. **f,** Antenna gain as a function of Δz at the corresponding resonance frequency. **g,** Radiated power as a function of Δz at the corresponding resonance frequency. **h,** Antenna radiation efficiency as a function of Δz at the corresponding resonance frequency. **i,** Antenna gain as a function of Δz at f = 9.8 GHz. **j,** Radiated power as a function of Δz at f = 9.8 GHz.**k,** antenna radiation efficiency as a function of Δz at f = 9.8 GHz.

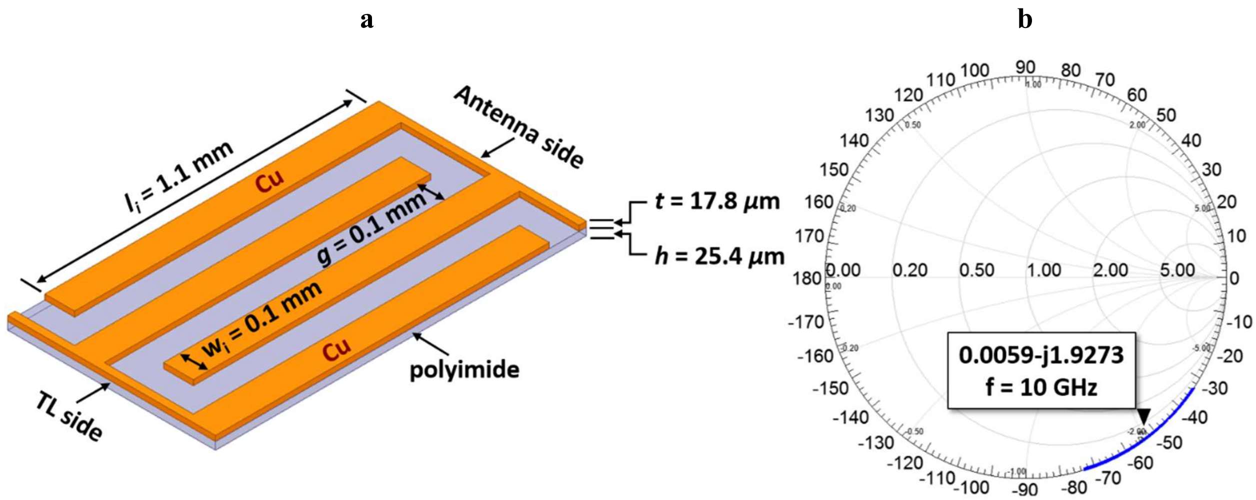

Supplementary Fig. 18 | FIMP antenna's interdigital capacitor section used for impedance matching and loading the antenna. a, Design layout. **b,** Extracted normalized impedance on the Smith chart.

Supplementary Table 1 | Resonance frequency and return loss values associated with each of the 16 elements of the flexible 4x4 phased array tile proof-of-concept prototype.

Excited element $i = 1, 2, \ldots, 16$	1	2	3	4	5	6	7	8	9	10	11	12	13	14	15	16
f_0 (GHz)	10.39	10.1	9.93	10.33	10.4	9.85	10.3	10.35	10.37	10.37	10.2	10	9.95	10.14	9.87	9.95
$\lvert S_{ii} \rvert$ (dB) $i = 1, 2, \ldots, 16$	-22	-22	-52	-48	-25	-22	-26	-27	-54	-42	-17	-24	-38	-27	-28	-31

Supplementary Table 2 | The 4x4 flexible phased array tile prototype simulated scattering parameter values ($S_{i,j}$, i, j = 1, 2, …, 16) at operation frequency f =9.8 GHz. ($S_{i,j}$, when $i = j$, represents return loss values highlighted by yellow color in the table, and $S_{i,j}$, when $i \neq j$, represents the cross coupling between the i-th and j-th elements.)

i \ *j*	1	2	3	4	5	6	7	8	9	10	11	12	13	14	15	16
1	-13.7	-22.6	-26.6	-28.6	-32.7	-39.2	-38.8	-38.4	-32.4	-40.5	-36.8	-32.4	-28.8	-28.5	-20.1	-19.7
2	-22.6	-13.2	-21.3	-30.7	-29.7	-43.9	-35.3	-35.9	-34.6	-39.7	-36.8	-34.3	-33.8	-33	-32.4	-26.4
3	-26.6	-21.3	-21.6	-27.7	-20.5	-29.7	-32.6	-35.1	-31.9	-36.7	-32.8	-31.7	-28.8	-33.2	32.7	-19
4	-28.6	-30.7	-27.7	-11.7	-18.3	-29	-19.4	-27.6	-18.8	-33	-28.1	-32.6	-27.5	-37.4	-33.2	-18.3
5	-32.7	-29.7	-20.5	-18.3	-15.2	-20.4	-28.8	-31.4	-28.3	-33.2	-30.9	-33.2	-31.1	-37.8	-37.2	26.9
6	-39.2	-43.9	-29.7	-29	-20.4	-21.6	-20.1	-29.1	-30.9	-30.3	-32.1	-37.3	-37.3	-41.9	-42.4	-33.1
7	-38.8	-35.3	-32.6	-19.4	-28.8	-20.1	-12	-19.1	-28.3	-29.6	-33	-36.9	-33	-41.2	-39.4	-28.6
8	-38.4	-35.9	-35.1	-27.6	-31.4	-29.1	-19.1	-16.7	-19.3	-19.6	-27.8	-33.3	-28	-38.5	-37.9	-32.3
9	-32.4	-34.6	-31.9	-18.8	-28.3	-30.9	-28.3	-19.3	-11.6	-27.3	-19.3	-27.7	-18.4	-33.1	-27.8	-27.5
10	-40.5	-39.7	-36.7	-33	-33.2	-30.3	-29.6	-19.6	-27.3	-22.8	-20.1	-26.5	-33.2	-37.3	-37.1	-37
11	-36.8	-36.8	-32.8	-28.1	-30.9	-32.1	-33	-27.8	-19.3	-20.1	-11.3	-19.7	-28.4	-29	-32.6	-32.2
12	-32.4	-34.3	-31.7	-32.6	-33.2	-37.3	-36.9	-33.3	-27.7	-26.5	-19.7	-16.1	-18.6	-21.4	-27.4	-28.6
13	-28.8	-33.8	-28.8	-27.5	-31.1	-37.3	-33	-28	-18.4	-33.2	-28.4	-18.6	-21.4	-26.4	-19.5	-19.3
14	-28.5	-33	-33.2	-37.4	-37.8	-41.9	-41.2	-38.5	-33.1	-37.3	-29	-21.4	-26.4	-13.9	-20.7	-38.5
15	-20.1	-32.4	-32.7	-33.2	-37.2	42.4	-39.4	-37.9	-27.8	-37.1	-32.6	-27.4	-19.5	-20.7	-25	-25.6
16	-19.7	-26.4	-19	-18.3	-26.9	-33.1	-28.6	-32.3	-27.5	-37	-32.2	-28.6	-19.3	-38.5	-25.6	-21.3

Supplementary Table 3 | Optimized phase setting for each radiating element (element i) of the 4x4 flexible phased array tile proof-of-concept prototype to perform beam-scanning towards the three chosen directions (φ=0°, θ=0°), (φ=0°, θ=30°), and (φ=90°, θ=30°).

Scan angle / Element	(φ=0°, θ=0°)	(φ=0°, θ=30°)	(φ=90°, θ=30°)
1	314.1°	206.1°	314.1°
2	28.9°	28.9°	28.9°
3	75.3°	75.3°	183.3°
4	138.5°	30.5°	354.5°
5	305.2°	305.2°	161.2°
6	93°	93°	57°
7	139.4°	31.4°	103.4°
8	108.8°	252.8°	72.8°
9	138.9°	282.9°	354.9°
10	90.9°	126.9°	54.9°
11	148.5°	184.5°	4.5°
12	49.9°	85.9°	157.9°
13	79.2°	223.2°	187.2°
14	31.4°	67.4°	31.4°
15	84.3°	228.3°	84.3°
16	83.6°	335.6°	191.6°

Supplementary Table 4 | The simulated and measured radiation characteristics summary of the 4x4 flexible phased array tile proof-of-concept when all 16 elements are turned ON for the three chosen scan angle phase settings: (φ=0°, θ=0°), (φ=0°, θ=50°) and (φ=90°, θ=30°). (The measured values are shown by blue color text and the simulated values are represented with black color text.)

			Normalized intensity (dB)	Largest sidelobe (dB)	Half-power beamwidth (deg)
(φ=0°, θ=0°)	simulation	E_θ, $\varphi = 0°$	-20.21	-20.21	—
		E_θ, $\varphi = 90°$	0	-12.54	22
		E_φ, $\varphi = 0°$	0	-14.31	21
		E_φ, $\varphi = 90°$	-36.99	-38.04	—
	Measurement	E_θ, $\varphi = 0°$	-18.19	-18.19	—
		E_θ, $\varphi = 90°$	-0.12	-10.92	23
		E_φ, $\varphi = 0°$	0	-11.09	20
		E_φ, $\varphi = 90°$	-24.64	-24.64	—
(φ=0°, θ=30°)	simulation	E_θ, $\varphi = 0°$	-10.14	-14.11	—
		E_θ, $\varphi = 90°$	-14.09	-24.38	—
		E_φ, $\varphi = 0°$	0	-10.58	24
		E_φ, $\varphi = 90°$	-29.09	-37.08	—
	Measurement	E_θ, $\varphi = 0°$	-13.33	-24.7	—
		E_θ, $\varphi = 90°$	-13.03	-14.04	—
		E_φ, $\varphi = 0°$	0	-11.55	25
		E_φ, $\varphi = 90°$	-28.33	-28.36	—
(φ=90°, θ=30°)	simulation	E_θ, $\varphi = 0°$	-31.51	-31.51	—
		E_θ, $\varphi = 90°$	0	-10.6	24
		E_φ, $\varphi = 0°$	-26.95	-18.65	—
		E_φ, $\varphi = 90°$	-39.88	-10.28	—
	Measurement	E_θ, $\varphi = 0°$	-21.77	-21.77	—
		E_θ, $\varphi = 90°$	0	-8.57	23
		E_φ, $\varphi = 0°$	-12.41	-9.25	—
		E_φ, $\varphi = 90°$	-29.03	-20.48	—

Supplementary Table 5 | The simulated and measured radiation characteristics summary of the 4x4 flexible phased array tile proof-of-concept when 12 elements are ON (corners elements turned OFF) for the three chosen scan angle phase settings: (φ=0°, θ=0°), (φ=0°, θ=50°) and (φ=90°, θ=30°). (The measured values are shown by blue color text and the simulated values are represented with black color text.)

			Normalized intensity (dB)	Largest sidelobe (dB)	Half-power beamwidth (deg)
(φ=0°, θ=0°)	simulation	E_θ, $\varphi = 0°$	-22.15	-22.15	—
		E_θ, $\varphi = 90°$	0	-25.44	45
		E_φ, $\varphi = 0°$	0	-35.11	47
		E_φ, $\varphi = 90°$	-38.44	-39.25	—
	Measurement	E_θ, $\varphi = 0°$	-20.08	-23.25	—
		E_θ, $\varphi = 90°$	0	-10.26	33
		E_φ, $\varphi = 0°$	-0.89	-14.65	42
		E_φ, $\varphi = 90°$	-22.61	-26.52	—
(φ=0°, θ=30°)	simulation	E_θ, $\varphi = 0°$	-10.32	-12.6	—
		E_θ, $\varphi = 90°$	-11.86	-12.07	—
		E_φ, $\varphi = 0°$	0	--12.05	51
		E_φ, $\varphi = 90°$	-27.26	-33.89	—
	Measurement	E_θ, $\varphi = 0°$	-12.65	-12.65	—
		E_θ, $\varphi = 90°$	-11.63	-11.63	—
		E_φ, $\varphi = 0°$	0	-10	48
		E_φ, $\varphi = 90°$	-27.54	-27.71	—
(φ=30°, θ=90°)	simulation	E_θ, $\varphi = 0°$	-20.59	-22.19	—
		E_θ, $\varphi = 90°$	0	-18.65	51
		E_φ, $\varphi = 0°$	-11.05	-18.65	—
		E_φ, $\varphi = 90°$	-36.06	-10.28	—
	Measurement	E_θ, $\varphi = 0°$	-18.55	-11.26	—
		E_θ, $\varphi = 90°$	0	-38.43	48
		E_φ, $\varphi = 0°$	-9.25	-9.25	—
		E_φ, $\varphi = 90°$	-20.48	-20.48	—